LUND UNIVERSITY

BACHELOR OF SCIENCE THESIS

DEPARTMENT OF NUCLEAR PHYSICS

Characterization of Double Sided Silicon Strip Detectors from LYCCA modules for FAIR

Author
Dalia Farghaly

Supervisor
Dr. Luis Sarmiento Pico
Co-supervisor
Dr. Pavel Golubev

LUND UNIVERSITY

June 18, 2019

Abstract

Begun in 2010, the Lund-York-Cologne-CAlorimeter, LYCCA, collaboration is targeted at discovering exotic nuclear reaction products whilst implementing the possibility of both position tracking and measuring residual energies of relativistic particles. Each LYCCA module is composed of a double sided silicon detector and 9 CsI(Tl) detectors. This project is primarily focused on the Si detectors, the main aim being charaterization of 10 such modules and making sure they are in satisfactory condition to be delivered to FAIR. Values for the leakage current at full depletion voltage were recorded and energy resolution were extracted. In addition to this, 18 32-channels Cologne-produced preamplifiers were tested to ensure they are fully functional. The data was acquired using a FEBEX-MBS fully digital data acquisition system and calibrated using a Gnuplot script. The energy resolution per strip on both p- and n- sides as well as the energy resolution as a function of energy were extracted using python. All 10 LYCCA modules tested in this work fulfilled the requirements in both energy resolution and leakage current and are fit for experimental use.

Acknowledgements

Firslty, I would like to thank Dr. Luis Sarmiento and Prof. Dirk Rudolph for sparking an interest within me in the field of nuclear physics, allowing me to have the oppurtunity to do this bachelor project even during the busiest of times, and taking time to proof read my drafts. My appreciation goes to Dr. Luis Sarmiento for always being willing to explain concepts and answer questions pedagogically, particularly about the data acquisition system, and Dr. Pavel Golubev for allowing me to witness every step of the production process and answer any questions I might have along the way, overall making this project a great and memorable experience. Thanks to Dr. Daniel Cox, who took the time to patiently explain how the calibration script works. Lastly, I would like to express my gratitude to my family for encouraging and supporting me throughout my period of studies.

Contents

List of Acronyms

- DSSSD: Double Sided Silicon Strip Detector
- LYCCA: Lund York Cologne CAlorimeter
- FAIR : Facility for Antiproton Ion Research
- NUSTAR: NUclear STructure, Astrophysics and Reactions
- HISPEC: High-resolution In-flight SPECtroscopy
- DESPEC: DEcay SPECtroscopy
- FRS: FRagment Separator
- AGATA: Advanced GAmma-ray Tracking Array
- MBS: Multi Branch System

Chapter 1

Introduction

One of the underlying aims of research in the field of nuclear physics is synthesizing and discovering new exotic nuclei, as well as studying their properties, such as ground states, excited states and decay modes. The structure of atomic nuclei gives an insight to questions about the conditions of the early universe, how matter works and how it was created. Some of the most rudimentary questions yet to be answered include: Where do heavy elements come from? Are there limits to the periodic table? How will these discoveries impact the nuclear shell model? The Lund-York-Cologne-CAlorimeter, LYCCA, was designed to shed some light on such inquiries.

LYCCA is an international collaboration with the aim to develop a high energy resolution calorimeter. LYCCA has already been used during the 2012 PRESPEC-AGATA campaign and will be used in the HISPEC/DESPEC campaigns, which are a part of FAIR under the NUSTAR umbrella. The beam to be used at FAIR is a very high intensity radioactive ion beam produced the driver accelerator which then passes through the state-of-the-art Super-Fragment-Separator, Super-FRS. The Super-FRS is a magnetic spectrometer of 71m in length, consisting of various bending and focusing magnets. This beam will be supplied to three branches, the Low Energy Branch, LEB, the High Energy Branch and the ring branch. The HISPEC experimental setup is located in the low energy cave along with the AGATA detector. [7]

AGATA is a 4π detector which makes use of electrically segmented high purity Germanium crystals to track the gamma rays produced from excited nuclear states in 3-dimensions. With the help of complex electronics systems as well as pulse shaping technologies, information about the energy and 3 dimensional points of interaction of the gamma rays with the segmented germanium can be collected. Advanced algorithms are constructed to extract the energy, time and position, allowing the structure of atomic nuclei at the limit of stability to be studied with respect to variables such as angular momentum, isospin and temperature. Overall, the HISPEC collaboration aims to examine nuclear reactions and structure with high resolution gamma ray spectroscopy. Information on vibrational or rotational characteristics of nuclei can help determine their shape while properties like ground, excited and high-spin states as well as transition probabilities can also be closely investigated. LYCCA is located behind this setup and is used to identify the reaction products. [1]

The low energy cave at FAIR is presently under construction. The commissioned LYCCA detectors characterized in this thesis are kept at the University of Cologne where they are configured with an alternative set-up at the tandem accelerator facility until they are needed for the HISPEC/DESPEC experiments at FAIR.

Chapter 2

A LYCCA module

The LYCCA telescopes are comprised of two different kinds of detectors: a semiconductor detector, in this case a DSSSD (Double Sided Silicon Strip Detector) and 9 Caesium-Iodide Thallium activated, CsI(Tl), crystals arranged in a 3x3 array. LYCCA's modular structure allows for a high degree of flexibility to be achieved as they can be arranged in various geometrical configurations. In HISPEC/DESPEC, the aim is to arrange them in a wall made of 26 detectors as this will minimize dead space in between the detectors as well as provide a good solid angle coverage.

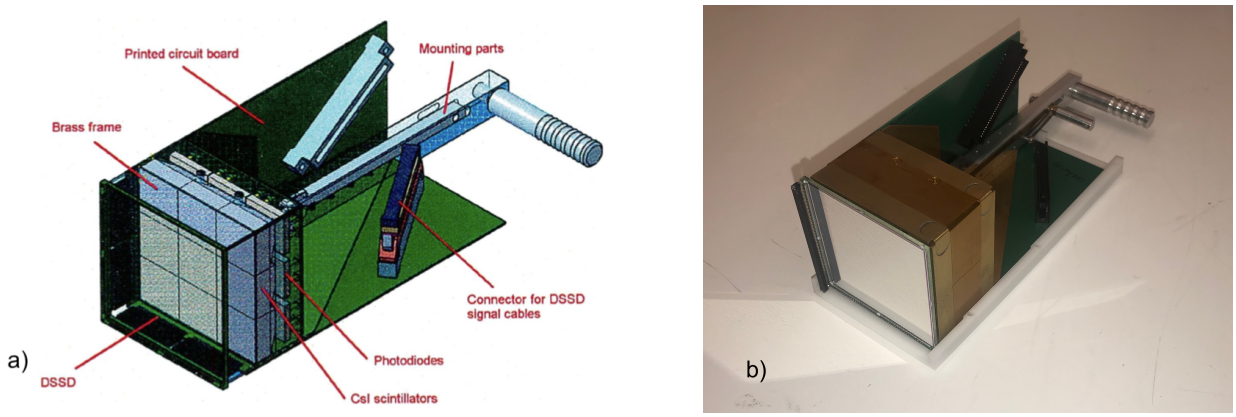

Figure 2.1: Figure (a) shows a schematic diagram of a LYCCA module. Figure (b) shows an assembled DSSSD in a LYCCA module.

LYCCA's main objective is to detect exotic nuclei with kinetic energies ranging between 100 MeV/u - 300 MeV/u produced in nuclear reactions[7], by measuring the residual energy loss ($E_{res} = E - \Delta$E) of particles colliding with the detector. The Bethe formula provides a good approximation for a high energy charged particle's mean energy loss per unit length of travel through matter, also known as "stopping power". Considering a particle at relativistic speed v, charge state z, mass m and energy E that hits a target with mean excitation potential I and electron density n after travelling a distance x, the stopping power per unit length of matter is:

$$-\left\langle \frac{dE}{dx} \right\rangle = \frac{4\pi}{m_e c^2} \cdot \frac{nz^2}{\beta^2} \cdot \left(\frac{e^2}{4\pi\epsilon_0}\right)^2 \cdot \left[\ln\left(\frac{2m_e c^2 \beta^2}{I \cdot (1-\beta^2)}\right) - \beta^2\right] \tag{2.1}$$

Where ϵ_0 is the vacuum permittivity, $\beta = \frac{v}{c}$, e is electronic charge, m_e is the rest mass of an electron and c is the speed of light in a vacuum. For a low energy charged particle travelling at non relativistic speeds, the factor $\beta << 1$. Another assumption made is that the mean excitation potential I is treated as a constant here, as it has been shown that it is in fact proportional to the atomic number Z; however, this proportionality is not significant an can be neglected. [2] The electron density of the target material can be calculated by the following equation:

$$n = \frac{N_A \cdot Z_t \cdot \rho}{A_r \cdot M_u} \tag{2.2}$$

Where N_A is Avogadro's number, Z_t is proton number of the target material, ρ is the density of the target material, A_r is the atomic weight and M_u is the molar mass constant.

Z of an incoming ion can be expressed as a function of ΔE and $E_{total,kinetic}$, which can displayed in a graph as shown in Figure 2.2. If the energy resolutions of both these quantities are in the neighbourhood of 1-2%, which the LYCCA collaboration aims to provide, the energy resolution for Z ($\frac{\Delta Z}{Z}$) will be sufficient to distinguish the number of protons in the reaction product. The 2-dimensional position recorded by the LYCCA module can provide the position of a charged ion with an uncertainty of $\pm$ 1mm on the plastic membrane. In order to find the atomic mass, A, the time of flight measurement is required to find the velocity of the ion. 2mm thick plastic-scintillator membranes in combination with 32 photomultiplier tubes each are used as start-stop detectors for this very purpose. [3] By assuming that the incoming radioactive ions are completely stripped and by using the ToF measurements to find the velocity, β, the mass, A, of the isotope can be determined. The biggest separations shown on the plot are due to the different charges, Z. A smaller separation between different Z values is due to mass differences, A. Refer to text for details. [3]

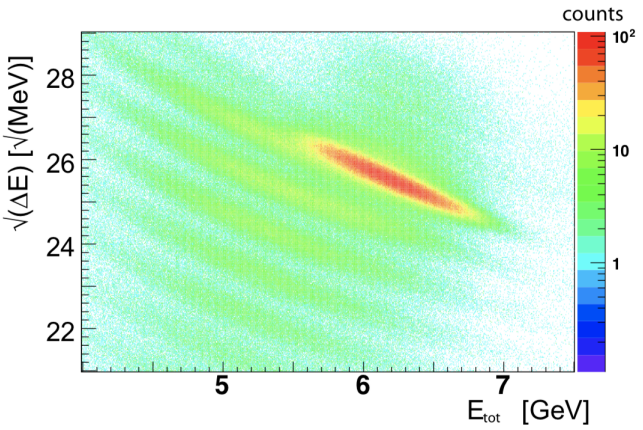

Figure 2.2: Z indenfication plot. [3]

The average energy deposition of a charged ion in a DSSSD is around 100 MeV. The kinetic energy of such a particle is the sum of the deposited energies at all the detection parts it goes through; this includes both the primary DSSSD target and DSSSD wall, the plastic scintillator membrane (40 MeV) and CsI crystals (4 GeV). As the particle is completely stopped by the CsI(Tl) crystal, the total kinetic energy can be retrieved. Relativistic corrections must be applied to the velocity ($\beta \approx 0.5$) and the Lorentz factor is determined. Then, by the energy-momentum correlation below the mass of the incoming projectile can be found. [3]

$$E_{total,kinetic} = m\gamma c^2 - mc^2 \tag{2.3}$$

Based on information from the FRS, the initial neighbourhood of the isotope is determined such that the mass resolution ($\frac{\Delta A}{A}$) can be determined in this region .

2.1 The DSSSD

DSSSDs are silicon crystalline semiconductor detectors which are able to measure the energy loss as well as track the incoming particle. The working principle of a semiconductor detector is based on its energy band structure and the presence of charge carriers. Due to the discrete nature of atomic levels, there is a valence band and a conduction band, between which there is a band gap where there are no energy levels for the electrons to occupy. Conduction and valence bands are essentially multiple individual energy levels which are distributed very closely, but since the semiconductor has a crystal lattice structure, it causes the wavefunctions of the electrons to overlap, making it possible to regard these energy levels as a continuum. [4] The spacing between atoms is what determines the thickness of the band gap, which in this case is approximately 1eV. When an electron is excited across a band gap, a positively charged electron hole forms in its place leading to an electron-hole pair. This is illustrated in Figure 2.3 below.

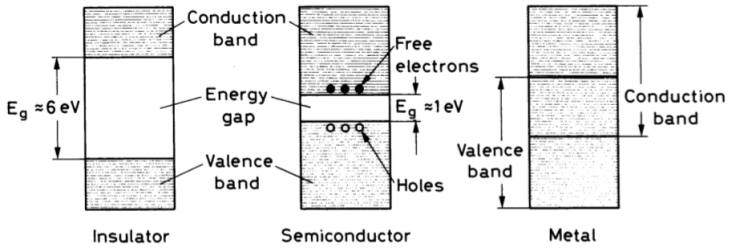

Figure 2.3: Comparison of band gap thickness between an insulator, semiconductor and conductor. [4]

In order to avoid the recombination of electron-hole pairs, an impurity is often introduced through a process called doping. By doing this, new acceptor and donor energy levels are created; for instance, Silicon is tetravalent so if it is doped with a trivalent or pentavalent impurity, there will be either an excess electron or electron hole left behind. These materials are referred to as n-type or p-type respectively. When p-type and n-type materials are placed in contact with each other, a depletion zone is created. At first, an initial current can be detected, since the electron holes travel towards the n-side and the electrons travel towards the p-side. There are no charge carriers present in the depletion zone and there is only a potential difference over the junction, allowing electrons and holes to drift in the electric field created.

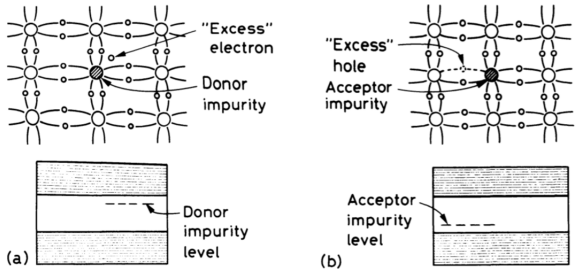

Figure 2.4: Acceptor and Donor levels after doping semiconductor [4].

The thickness of the depletion zone is moderated by the contact potential, however it is not very capable of detecting radiation well, as the electric field is not strong enough. To improve the performance, a reverse bias over the junction can be applied, which will increase the width of the depletion zone. This can be more easily increased if the material has a high resistivity as seen in the formula below for holes:

$$\frac{1}{\sigma} = en_i\mu_e + \mu_h \tag{2.4}$$

where n_i is the charge carrier density, and μ_e and μ_h are the mobilities of the electrons and electron holes respectively [4].

Any incoming ionizing radiation creates electron-hole pairs and so a pulse with amplitude proportional to the radiation energy deposited in the material. The DSSSD is made primarily from an ion implanted, silicon-dioxide passivated wafer which is approximately 300 μm thick, enough to fully stop an incoming alpha particle. There is a layer of aluminium for electrical conductivity. It is 60.1 $\times$ 60.1 mm^2 wide, has an active area of 58.5 $\times$ 58.5 mm^2 and has 32 strips on each side. On the p-side the distance between the strips is 30 μm. However, as discussed before, capacitance and resistivity are important characteristics that influence the performance of the DSSSD and occurrence of noise; hence, to isolate the individual strips on the n-side (also called the ohmic side) additional p+ (heavily doped) zones are implanted between the adjacent n-type strips, increasing the inter strip distance to 200 μm. The strips on the p-side are orthogonal to the ones on the n-side, creating a grid of pixels which can track the incoming particles in 2-dimensions. The voltage required to fully deplete such a detector is 50 V. [11]

An important effect to consider is the leakage current, which may occur due to increase in temperature, condition of the detector's active area $etc.$ An increased leakage current may be an indication of radiation damage which can lead to significant degradation in energy resolution. In order to reduce the leakage current, several precautions can be taken, such as creating guard ring structures in order to avoid the possibility of leakage paths between the strips [5].

2.2 A CsI(Tl) Detector

A scintillator is a luminescent type of material which when exposed to ionizing radiation absorbs it and re-emits the energy in the form of optical light. The CsI(Tl) detectors in LYCCA provide a measurement of the total kinetic energy of incoming charged particles. Cs(Tl) has a light output of 54 photons per absorbed keV emitting most of them in the region of 550 nm [13]. This makes it compatible for the use of photodiodes as they reach a peak quantum efficiency of 82% around 560 nm [13]. In order to optimize the light collection and prevent light leakage between the individual crystals, each crystal is wrapped in a single layer of VM2000 foil. After this, they are wrapped once more in aluminium foil. 9 CsI(Tl) crystals are mounted behind each DSSSD [3]. Currently there are two geometries of CsI(Tl) crystals, a short and long type, measuring 13 mm and 33 mm respectively; yet only the shorter version is to be used in the upcoming HISPEC/DESPEC campaigns, due to the type of beams used. [12] In this thesis however, only the DSSSDs are characterized.

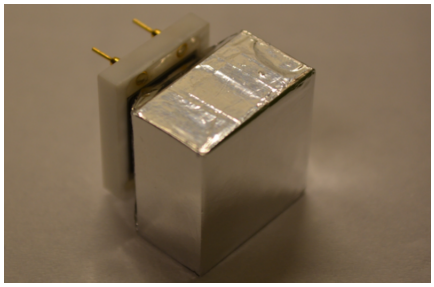

Figure 2.5: A short-type CsI(Tl) crystal wrapped in VM2000 foil, photo diode mounted with use of optical epoxy. [6]

2.3 DSSSD Preparation

The bare silicon wafers are delivered from RADCON Ltd, Zelenograd, Russia and must be prepared before usage. Firstly, the silicon strip detectors are mounted onto a FR4 frame made from printed circuit board material [11]. After the frame is attached, they must be placed in stainless steel holders as part of preparation before they undergo a process called “bonding”.

Bonding is done with the use of a bonding machine and it involves attaching a thin aluminum-silicon wire from the gold-plated pad on the board to the aluminum surface on the silicon detector. In principle, it is most optimal for the wires to be as short as possible, however due to some mechanical movement of the detector when it is in use, it is beneficial to have the wires slightly longer and not so taut. After the DSSSD has been bonded, the bonds must be secured by using a mix of epoxy and silver glue. A small amount of glue is placed on to the ends of each of the bonded wires, after which the detector is placed into an oven at 70 degrees Celsius for a few hours to accelerate the glue drying process. The connections are verified with the use of a voltmeter. Next, the pin-like connectors must be placed into the holes in the frame and tin-soldered, and finally the entire structure can be removed from the stainless steel holder. The DSSSD is then finally connected to the circuit board and is ready to be characterized [12].

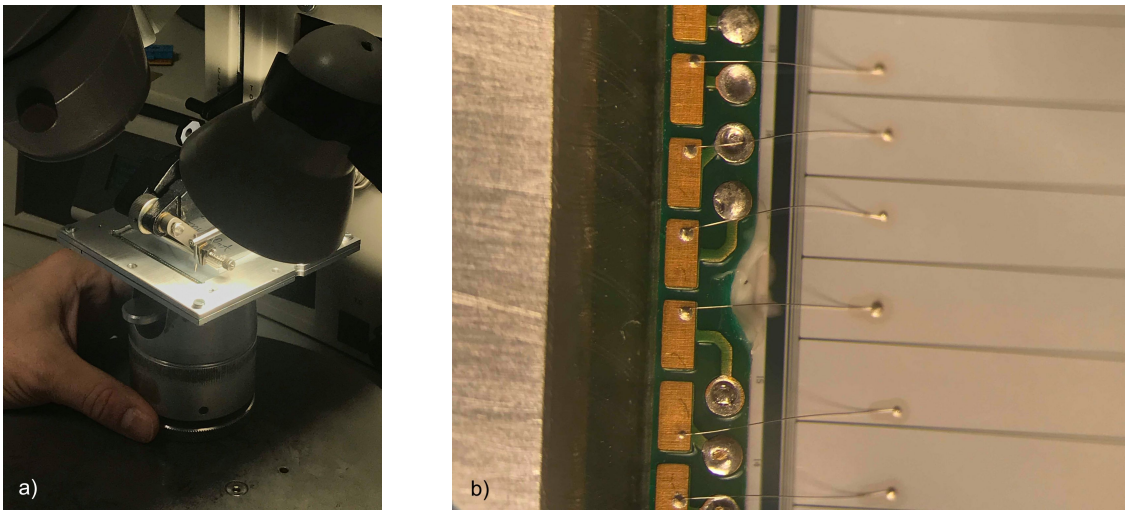

Figure 2.6: Figure (a) shows the DSSSD mounted on the stainless steel frame during the bonding process. Figure (b) shows the bonded wires attached to the DSSSD with epoxy-silver glue

Chapter 3

Testing the DSSSDs

The main aim of LYCCA is to detect and identify the products from the nuclear reactions by measuring the 2-dimensional position ((x, y)), energy loss ($\Delta E - E$) and time of flight (ToF) before and after the secondary target. The timing information is collected using 3 plastic membranes with multi-PMT readout schemes. In this thesis however, only the DSSSDs will be tested, characterized and checked against the standard set by the LYCCA Technical Design Report.[10]

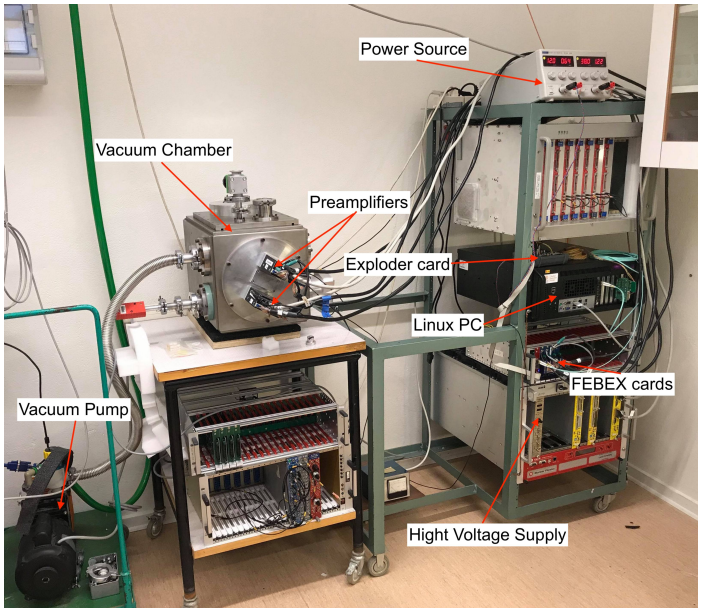

Figure 3.1: The experimental setup

The test was carried out at the local laboratory of the Nuclear Structure Group. The setup has two parts. First, a vacuum chamber containing a radioactive source and the LYCCA module itself, the second part is the FEBEX readout electronics and the MBS data acquisition system (DAQ).

All the measurements were performed under the same conditions. The radioactive source used was Thorium-228, which was placed in the vacuum chamber and placed at a marked distance 8 cm away from the detector. The 32+32 signals (p- and n-side) were connected to two 32-channels Cologne-produced preamplifiers. The DSSSDs were biased with 50 V coming from a NIM power supply where the leakage current was also displayed. The energy signals were connected to four FEBEX3 digitizer cards (operated at 50 MHz sampling rate) and the data was read out via an MBS-enabled PC connected with an optical link. Online data monitoring was done using the GSI Go4 [15] software based on ROOT [14]. Offline data manipulation (peak fitting) was done using Gnuplot [16].

3.1 The Data Acquisition system

The Multi Branch System, MBS data acquisition system used here was developed in Darmstadt, Germany in the experiment electronics department of GSI. In an analog readout system like the one shown in Figure 3.1 the pulses must be shaped before undergoing any further processing. An analog-to digital converter, as the name suggests, converts analog signals coming from the shaper to digital signals which are proportional to the height of the input, i.e. the energy deposited into the detector. The digital signals from the ADC must be sorted, this is done by the Multi-Channel Analyser, MCA. In this case the function of an MCA was performed with the use of Go4.

Whenever there is a high detection rate, the pulses may pile up and overlap, as one pulse's tail may interfere with the amplitude of another pulse which leads to incorrect results. Most modern DAQs circumvent this by using digitizer cards designed to perform the functions of a shaper and an analog-to-digital converter (ADC). In this case 4 FEBEX3 digitizer cards were employed. This allows us to perform signal processing routines directly in the digitized pulses regardless of whether they had overlaps or not.

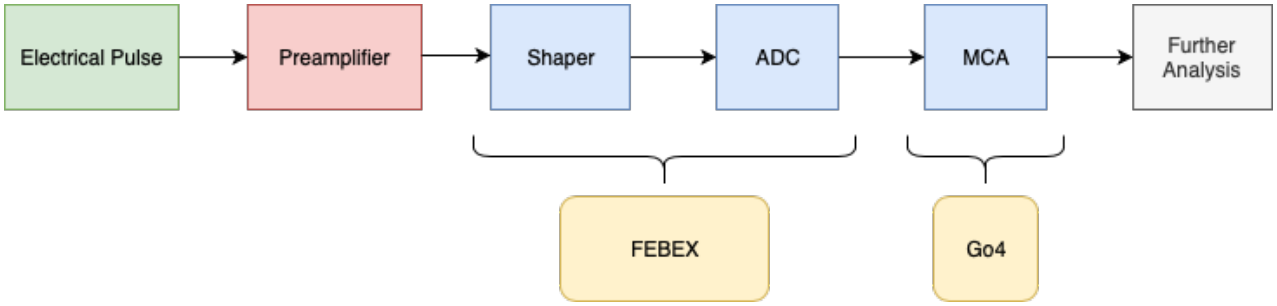

Figure 3.2: Flowchart of a traditional DAQ.

A FEBEX crate with four FEBEX3 cards, each one having 16 differential analog inputs. Cards numbered 0 and 1 are connected to the preamplifier which is in turn connected to the p-side of the detector, similarly cards 2 and 3 are connected to the preamplifier coming from the n-side. This way there are 64 FEBEX channels, each one corresponding to a single strip on the DSSSD which produces a spectrum like the one seen in Section 4, Figure 4.2.

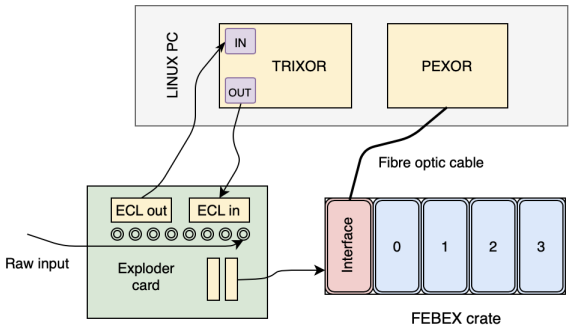

Figure 3.3: A basic MBS system such as the one used in this experiment.

A dual power source is used with 38 V going into the FEBEX cards as required and 12 V being supplied to the exploder module. Clock distribution, deadtime locking and trigger handling of the system is done by the EXPLODER card. Figure 3.2 above shows the set-up of the electronics used.

3.2 The Cologne Preamplifiers

In charge sensitive preamplifiers, such as the ones used in this thesis, the output voltage is proportional to the charge accumulated at the terminals during a given interval of time. Noise is specified as the FWHM of the peak purely due to the preamplifier and depends heavily on the input capacitance, which can come from the detector itself or the surroundings. Another function these preamplifiers is supplying the bias voltage to the detector. [5] In this thesis, preamplifiers of two different dynamic ranges will be tested: x1 gain and x3 gain. Each detector is connected to 2 preamplifiers with 32 channels each. They are manufactured in the Cologne electronics workshop according to LYCCA/Lundium specifications. To test the preamplifiers, a pulser is connected into the test input and the signals are read through a differential output to which an oscilloscope is connected through a differential probe. This is done to ensure all channels are responsive and the peaks are amplified appropriately, depending on whether the gain is x1 or x3.

Figure 3.4: A 15/45 MeV gain Cologne manufactured pre-amplifier.

Chapter 4

Results

The main objective of this bachelor thesis is to extract the energy resolution of each detector, and verify that it is within the specifications such that it qualifies for experimental use at HISPEC/DESPEC. The current criteria requires a minimum energy resolution of $< 1\%$ with a goal of 0.5% and leakage current of less than 2 μA [10], [12].

The energy resolution for a single strip as a function of energy is also obtained. After the data has been successfully acquired and written to a file, Go4 was used to sort the data and extract the raw spectra of Thorium-228, per strip as well as pixel. These spectra were then calibrated for each strip using a script in gnuplot to fit a Gaussian curve to 4 alpha decay peaks of energies: 5685keV which comes from Radium-224 decaying into Radon-220 , 6288keV caused by its decay into Polonium-216, 6778keV from Polonium-216 to Lead-212, and finally 8784keV from Polonium 212 to Lead-208. This was done for each strip on both (32x) n- and (32x) p- sides for all 10 detectors. Figure 4.1 shows the complete decay sequence of Th-228 including the branching ratios. Other peaks of significant probabilities were omitted during calibration due to insufficient energy resolution.

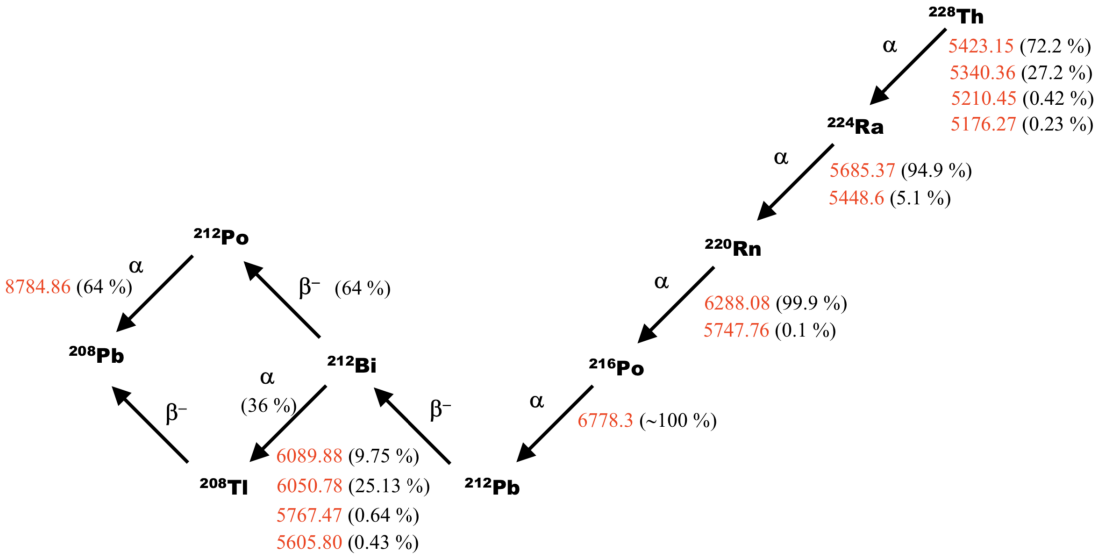

Figure 4.1: The decay sequence of Thorium-228 [17]

4.1 Energy Resolution

The alpha particles emitted by the Th-228 source are fully stopped by the silicon wafer, which makes it a suitable choice for this characterization. Alpha particles of energy 8784 keV are used to extract the energy resolution per strip. The energy resolution as a function of energy is also calculated. A Gnuplot script was used to calibrate spectra such as the one in Figure 4. and was modified to output all the necessary information such as sigma for all the peak energies, $\sigma = FWHM/2.355$, as well as peak positions in channels. If the centroid of the peak is known, the FWHM can then be calculated for each strip. The energy resolution per pixel is better than per strip since the incoming particles penetrating the dead layer at different angles experience different thickness; causing a larger spread in energies collected.

The energy resolution (FWHM) for each strip on both the p-side and n-side at an energy of 8784keV were obtained (see Appendix) and were plotted for Wafer-10 in Figures 4.4 and 4.5. 3 channels out of 64 were displaying a strange behaviour: channel 8 on FEBEX card 1, which has been removed from the graphs, and channels 12 and 13 on FEBEX card 3, all corresponding to strips 24, 61 and 62 respectively. It has been verified that this behaviour is attributed to the FEBEX system because it is a recurring pattern on all the DSSSDs, and all channels were checked with an oscilloscope to ensure they are responsive and have a comparable amplitude to the other strips.

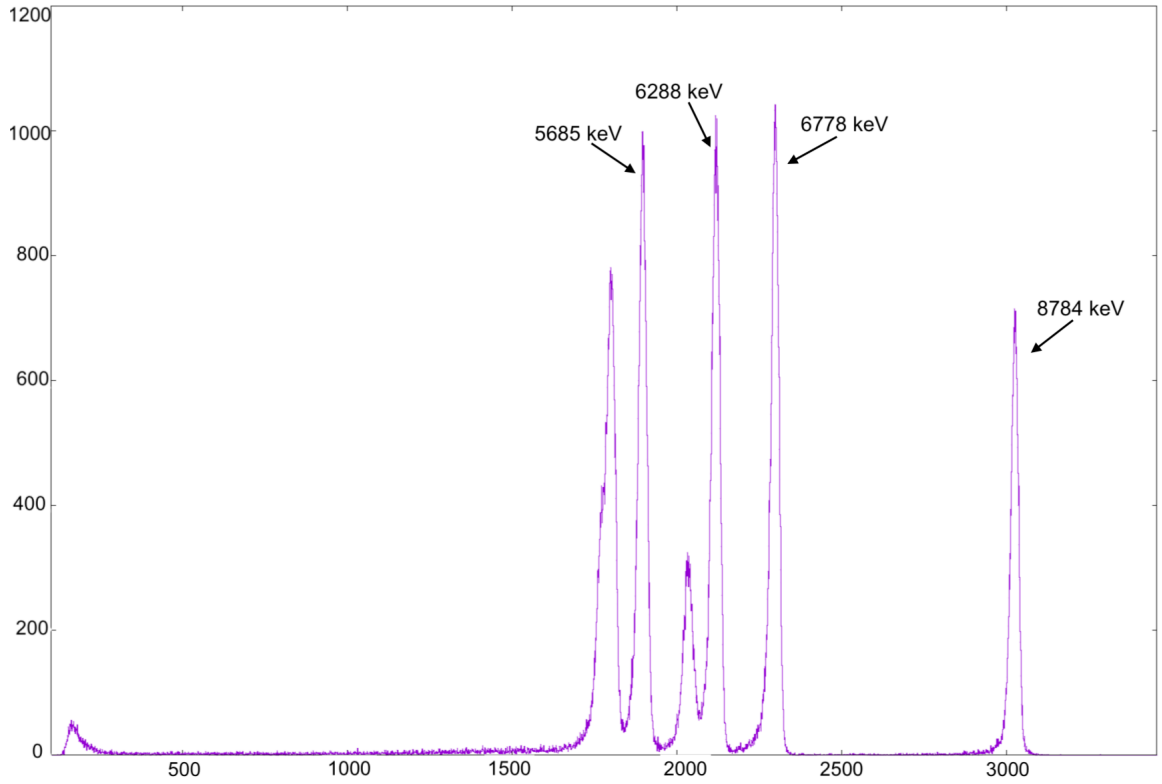

Figure 4.2: Uncalibrated spectrum of strip number 14 on DSSSD "Wafer-10". Arrows indicate peaks used in calibration.

The calibration function in the form of $E = a \cdot ch + b$, for each detector can be calculated. Figure 4.3 shows that the energy resolution improves as energy increases. This suggests that the energy resolution is even better at higher energy physics experiments such as HISPEC.

Plots such as the one in Figures 4.4 and 4.5 show the energy resolution per strip on the p-side as well as n-side. All strips are functional and have an energy resolution of approximately in the neighbourhood of 1%. Knowing the energy resolution per strip can give insight regarding the positioning of the detectors in the final setup; i.e. which modules are more suitable to be placed in the center or outer corners of the LYCCA wall. Having a good energy resolution is also an advantage in minimizing the dead time of the detector. The ending strips also generally display worse energy resolution than the ones in the middle as seen here; this is due to the fact that the wafers are cut from a larger piece using a laser which can impact the crystal lattice structure of the silicon. An error estimate for the energy resolution was calculated to be of the order $\pm$ 0.0001.

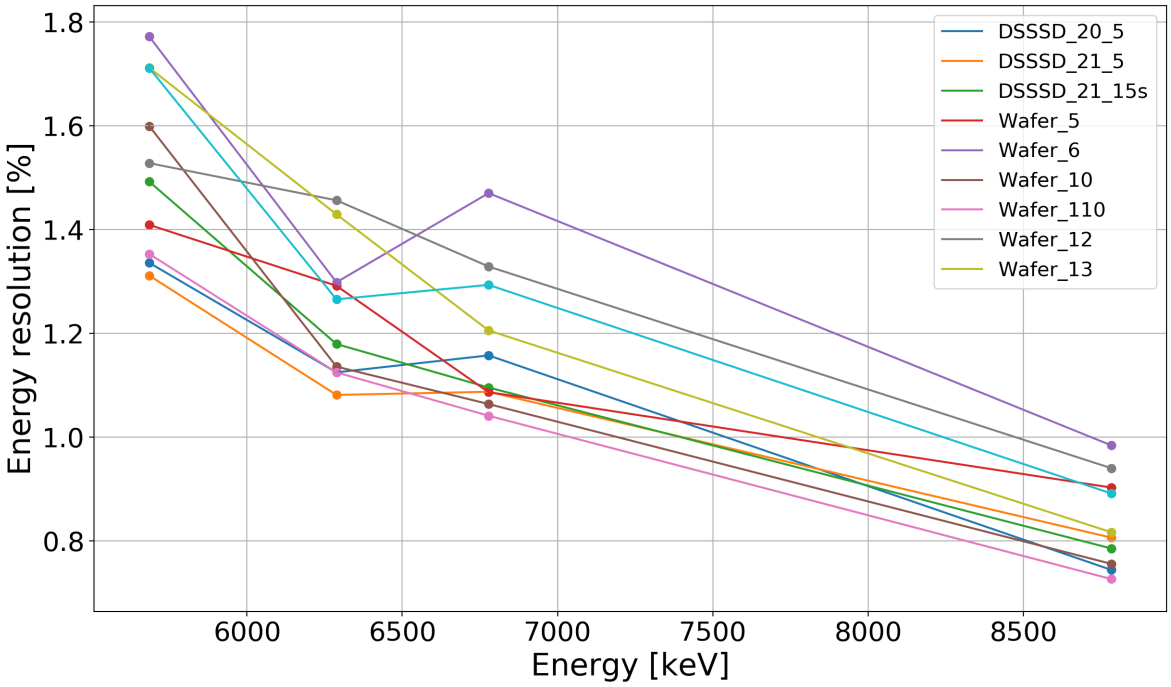

Figure 4.3: Energy resolution as a function of energy for a representative strip (strip number 14) for all DSSSDs

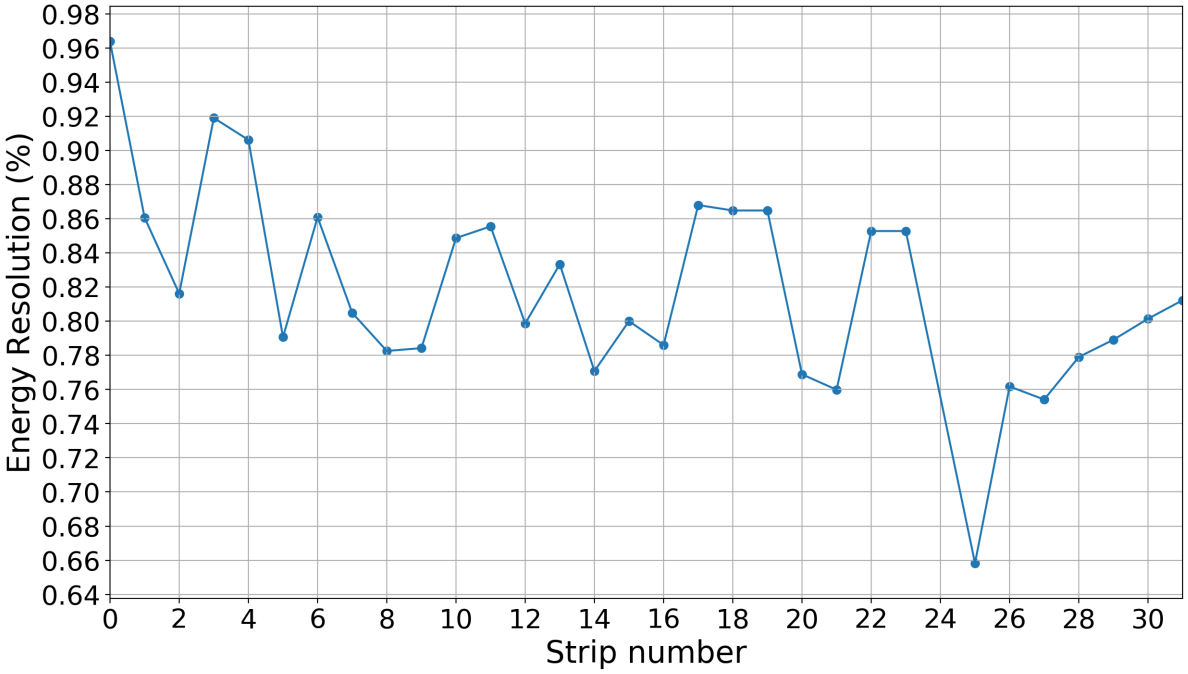

Figure 4.4: Plot showing the energy resolution per strip of detector "Wafer-10" for the p-side.

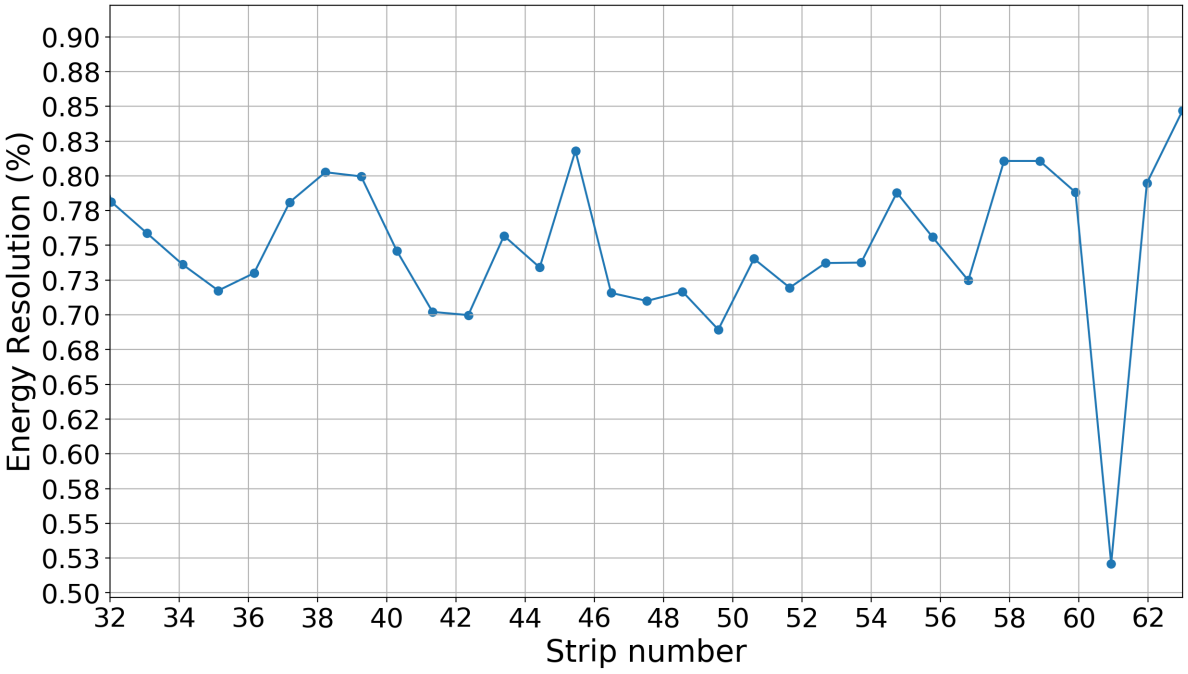

Figure 4.5: Plot showing the energy resolution per strip of detector "Wafer-10" for the n-side.

4.2 Leakage current

DSSSD name	Leakage Current (nA)
DSSSD N21-3	90
DSSSD 21-5	101
DSSSD 20-7	147
DSSSD 21-15	200
Wafer-5	66
Wafer-6	88
Wafer-10	104
Wafer-12	94
Wafer-13	102
Wafer -110	142

Table 4.1: Table displaying leakage current for each detector at 50V.

A silicon detector behaves like a diode, and reaches saturation point at a certain voltage, known as the depletion voltage. The DSSSDs used here are fully depleted at 50 V [11]; this is to ensure that they are fully depleted. It is recommended that the leakage current does not exceed 2 μA, before the detector needs to be annealed. A large leakage current can among other reasons be attributed to the imperfections in the crystal structure of the silicon; which can be due to radiation exposure or manufacturing imperfections. Annealing is a process that involves supplying thermal energy to the DSSSDs, which allows the dislocated atoms in the crystal structure to rearrange accordingly. Temperature is also another possible reason for an increased leakage current; however all measurements in this work were performed at room temperature. As seen from Table 4.1 the leakage current does not exceed 2 μA, so annealing was not required.

4.3 Testing the Preamplifiers

As a side investigation, 18 Cologne manufactured preamplifiers were tested using an oscilloscope. The two types tested included a 15/45 MeV and 7/21 MeV gain. All of them were confirmed to be fully functional on settings gain x1 as well as x3, and data has been collected from both types using a Th-228 source and detector “Wafer-10”, such that the dynamic range can be investigated further.

Chapter 5

Conclusion and Outlook

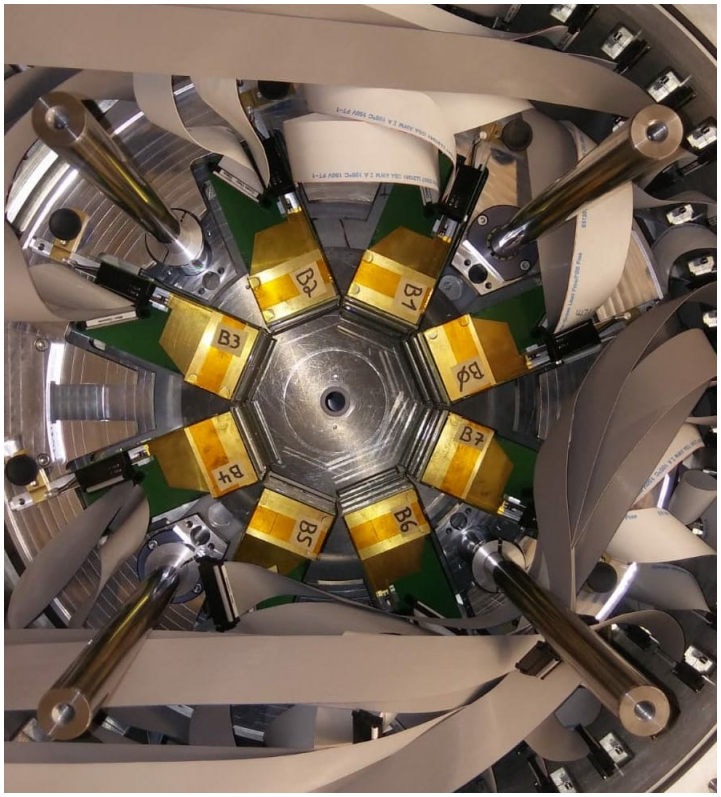

Figure 5.1: The detector setup inside the vacuum chamber at the accelerator facility in the University of Cologne

Overall this thesis work concluded that all 10 detectors tested are fit for experimental use; and that the energy resolution is sufficient for the HISPEC campaign. The data showed that all detectors have an energy resolution below 1% for alpha particles at an energy of 8784 keV. Experimental conditions such an imperfect vacuum or noise from the electronics may have contributed to this result. The energy resolution is also shown to increase with energy, which is an advantage considering the detectors will be used in high energy physics experiments. The data was calibrated and an error estimate was calculated, however no further error propagation was performed. The leakage currents were shown not to exceed 2 μA. Dead layer thickness per pixel for each of the detectors can also be extracted as part of further characterization, but in order to do this data from an electron source must be obtained. In total, twenty four modules have been manufactured with an aim to produce and characterize ten more.

Until FAIR is ready to accommodate the LYCCA modules, they are being held at the tandem accelerator facility in Cologne, where in May 2019, the Hoyle-State of Carbon-12 will be examined. The nucleosynthesis of C-12 undergoes a sequence of events known as the triple alpha process. Under high temperatures and pressures, two Helium atoms fuse together to form Beryllium-8; which is highly unstable with a half life of 6.7×10^{-17}s. This means a third alpha particle must

fuse with Beryllium-8 before it decays in order to produce a stable Carbon-12 nucleus. This seems to have an extremely small probability of occurring but since Beryllium-8 nucleus needs exactly the energy equivalent to one more Helium nucleus in order to form the Carbon-12 nucleus, there is a "resonance" which greatly increases the probability of fusion for a third time. Thus a stable Carbon-12 nucleus is formed in what is referred to as the Hoyle-State. The experiment aims to study the geometry of this alpha clusterization with the help of position sensitive detectors such as these DSSSDs. The configuration of the DSSSD detectors used is shown in Figure 5.1. Twenty two modules were used in total in an octagonal configuration.

Overall, this thesis aims to highlight both the functionality and importance of LYCCA, and explore how it works in detection of exotic nuclei.

Bibliography

[1] S. Akkoyun et. al. *AGATA—Advanced GAmma Tracking Array. Nuclear Instruments and Methods in Physics Research Section A: Accelerators, Spectrometers, Detectors and Associated Equipment*; 2012; 668; 26 - 58.

[2] Segrè, E. *Experimental nuclear physics. Wiley; 1953*

[3] Andreas Wendt *Isospin symmetry in the sd shell: Coulumb excitation of Ar-33 at relativistic energies and the new 'Lund-York-Cologne-Calorimeter 2013*

[4] Leo, William. R; *Techniques for nuclear and particle physics experiments : a how-to approach; Springer; 1994*

[5] Glenn F. Knoll; *Radiation detection and measurement; John Wiley; 2010*

[6] Barann, Anna Sophie; *Characterisation of LYCCA ΔE-E-Telescopes; 2013*

[7] Namita Goel; accessed April 2019; *HISPEC (high-resolution in-flight spectroscopy)/DESPEC (decay spectroscopy)*. https://fair-center.eu

[8] Epoxy Technology Inc, 2018; accessed May 2019; *Electrically Conductive Silver Epoxy, Technical Data Sheet*; www.epotek.com

[9] Dr. Ivan Rusanov; 2014; accessed April 2019; *Febex data acquisition system, Experiment-Elektronik GSI, Darmstadt*; https://wiki.gsi.de

[10] D Rudolph; *LYCCA, theLund-York-CologneCAlorimeter: Identication of reaction products in HISPEC-DESPEC@NuSTAR*; accessed April 2019

[11] P Golubev et. al; *The Lund-York-Cologne Calorimeter (LYCCA): Concept, Design and Prototype Developments for a FAIR-NUSTAR Detector System to Discriminate Relativistic Heavy- ion Reaction Products; Nuclear Instruments & Methods in Physics Research. Section A: Accelerators, Spectrometers, Detectors, and Associated Equipment; 2013*

[12] P. Golubev; *Private communication; 2019*

[13] Huusko, Alexander; *Commissioning of the ΔE-E LYCCA detector array; 2017*

[14] Root data analysis framework; accessed April 2019; https://root.cern.ch

[15] Go4 data analysis framework; accessed April 2019; https://gsi.de

[16] Gnuplot graphing utility; acessed April 2019; http://gnuplot.sourceforge.net

[17] Certificate of calibration alpha standard source; accessed April 2019; https://groups.nscl.msu.edu/hira/

[18] N. Kurz; The General Purpose Data Acquisition System MBS at GSI; 2011; accessed April 2019; http://lnr.irb.hr

Chapter 6

Appendix

Table 6.1: Energy Resolution per strip for detector “Wafer - 12”

Strip number	Energy Resolution [%]
0	0.909
1	1.004
2	0.945
3	0.978
4	0.864
5	0.952
6	0.905
7	0.923
8	0.948
9	0.875
10	0.934
11	0.954
12	1.031
13	1.003
14	0.970
15	0.999

Strip number	Energy Resolution [%]
16	0.876
17	0.942
18	0.947
19	0.947
20	1.004
21	0.863
22	0.922
23	0.922
24	1.843
25	0.958
26	1.045
27	0.937
28	0.994
29	0.825
30	0.907
31	1.024

Strip number	Energy Resolution [%]
32	0.939
33	0.885
34	0.890
35	0.885
36	0.764
37	0.860
38	0.886
39	0.886
40	0.891
41	0.891
42	0.900
43	0.772
44	0.814
45	0.758
46	0.759
47	0.827

Strip number	Energy Resolution [%]
48	0.738
49	0.803
50	0.843
51	0.815
52	0.782
53	0.904
54	0.806
55	0.794
56	0.881
57	0.773
58	0.776
59	0.776
60	0.698
61	0.845
62	0.754
63	0.877

Table 6.2: Energy Resolution per strip for detector “Wafer - 5”

Strip number	Energy Resolution [%]
0	0.965
1	0.920
2	0.826
3	0.778
4	0.815
5	0.945
6	0.831
7	0.969
8	0.900
9	0.983
10	0.874
11	0.933
12	1.057
13	0.962
14	0.817
15	0.949

Strip number	Energy Resolution [%]
16	0.954
17	0.912
18	0.900
19	0.983
20	0.786
21	0.910
22	0.860
23	0.856
24	0.874
25	0.914
26	0.914
27	0.946
28	0.850
29	0.850
30	0.784
31	0.765

Strip number	Energy Resolution [%]
32	0.812
33	0.812
34	1.826
35	0.884
36	0.808
37	0.765
38	0.894
39	0.915
40	0.882
41	0.959
42	0.946
43	0.895
44	0.878
45	0.827
46	0.870
47	1.179

Strip number	Energy Resolution [%]
48	0.933
49	1.343
50	0.851
51	0.996
52	0.998
53	0.875
54	0.913
55	0.944
56	1.817
57	0.933
58	0.933
59	0.845
60	0.751
61	1.021
62	0.816
63	0.823

Table 6.3: Energy Resolution per strip for detector "DSSSD 21-15"

Strip number	Energy Resolution [%]
0	1.047
1	0.774
2	0.890
3	0.852
4	1.011
5	0.927
6	0.789
7	0.781
8	0.931
9	0.862
10	0.888
11	0.961
12	0.861
13	0.903
14	0.880
15	0.826

Strip number	Energy Resolution [%]
16	0.792
17	0.914
18	0.848
19	0.848
20	0.932
21	0.815
22	0.997
23	0.791
24	1.830
25	0.938
26	0.844
27	0.798
28	0.949
29	0.936
30	0.817
31	0.888

Strip number	Energy Resolution [%]
32	0.871
33	0.899
34	0.908
35	0.789
36	0.794
37	0.789
38	0.868
39	0.875
40	0.852
41	0.757
42	0.891
43	0.838
44	0.772
45	0.834
46	0.826
47	0.785

Strip number	Energy Resolution [%]
48	0.785
49	0.765
50	0.767
51	0.923
52	0.860
53	0.896
54	0.864
55	0.794
56	0.951
57	0.894
58	0.893
59	0.897
60	0.826
61	0.715
62	1.007
63	0.941

Table 6.4: Energy resolution per strip for detector ”DSSSD 20-5”

Strip number	Energy Resolution [%]
0	0.930
1	0.825
2	0.824
3	0.855
4	0.838
5	0.862
6	0.894
7	0.874
8	0.811
9	0.812
10	0.830
11	0.849
12	0.902
13	0.755
14	0.830
15	0.782

Strip number	Energy Resolution [%]
16	0.768
17	0.867
18	0.774
19	0.774
20	0.899
21	0.763
22	0.829
23	0.829
24	1.830
25	0.764
26	0.923
27	0.912
28	0.959
29	0.953
30	0.897
31	0.915

Strip number	Energy Resolution [%]
32	0.837
33	0.833
34	0.869
35	0.827
36	0.747
37	0.727
38	0.859
39	0.757
40	0.744
41	0.844
42	0.844
43	0.676
44	0.712
45	0.730
46	0.720
47	0.748

Strip number	Energy Resolution [%]
48	0.748
49	0.821
50	0.801
51	0.786
52	0.871
53	0.700
54	0.759
55	0.760
56	0.815
57	0.826
58	0.828
59	0.828
60	0.978
61	0.769
62	0.820
63	0.819

Table 6.5: Energy Resolution per strip for detector “Wafer 6”

Strip number	Energy Resolution [%]
0.	1.062
1.	0.903
2.	0.884
3.	0.968
4.	0.908
5.	0.906
6.	0.950
7.	1.033
8.	0.939
9.	0.968
10	1.210
11	0.966
12	0.936
13	1.038
14	1.091
15	1.031

Strip number	Energy Resolution [%]
16	0.868
17	0.972
18	0.864
19	0.864
20	0.946
21	0.877
22	1.069
23	1.069
24	1.823
25	0.848
26	0.988
27	0.887
28	0.860
29	0.886
30	0.909
31	0.876

Strip number	Energy Resolution [%]
32	0.840
33	0.998
34	0.968
35	0.946
36	0.969
37	0.954
38	0.858
39	0.858
40	0.770
41	0.848
42	0.835
43	0.778
44	0.797
45	0.869
46	0.783
47	0.923

Strip number	Energy Resolution [%]
48	0.899
49	0.850
50	0.955
51	0.817
52	0.927
53	0.844
54	0.779
55	0.889
56	0.862
57	0.909
58	0.875
59	0.888
60	0.922
61	1.351
62	0.918
63	0.756

Table 6.6: Energy Resolution per strip for detector ”DSSSD N21 - 3”

Strip number	Energy Resolution [%]
0	0.982
1	0.783
2	0.856
3	0.766
4	0.878
5	0.989
6	0.872
7	1.082
8	0.866
9	0.792
10	0.877
11	0.780
12	0.810
13	0.976
14	0.777
15	0.936

Strip number	Energy Resolution [%]
16	0.982
17	0.986
18	0.978
19	0.819
20	0.791
21	0.889
22	0.963
23	0.919
24	1.829
25	0.984
26	0.969
27	0.917
28	0.958
29	0.873
30	1.066
31	0.851

Strip number	Energy Resolution [%]
32	0.797
33	0.850
34	0.950
35	0.856
36	0.903
37	0.917
38	0.829
39	0.722
40	0.918
41	0.714
42	0.714
43	0.894
44	0.859
45	0.890
46	0.811
47	0.786

Strip number	Energy Resolution [%]
48	0.786
49	0.801
50	0.892
51	0.889
52	0.826
53	0.823
54	0.841
55	0.868
56	0.728
57	0.731
58	0.865
59	0.865
60	0.620
61	0.966
62	0.773
63	0.957

Table 6.7: Energy Resolution per strip for detector “Wafer - 13”

Strip number	Energy Resolution [%]
0	1.133
1	0.990
2	0.887
3	0.949
4	1.096
5	0.873
6	0.905
7	1.066
8	0.852
9	0.911
10	1.029
11	0.970
12	0.958
13	0.963
14	0.928
15	0.868

Strip number	Energy Resolution [%]
16	0.994
17	1.011
18	1.170
19	0.991
20	1.061
21	0.991
22	0.971
23	0.971
24	1.447
25	1.120
26	1.106
27	1.042
28	1.039
29	1.166
30	1.193
31	1.267

Strip number	Energy Resolution [%]
32	1.405
33	1.055
34	1.111
35	0.933
36	1.052
37	0.952
38	1.136
39	1.136
40	0.942
41	0.942
42	0.827
43	1.001
44	1.023
45	0.878
46	0.886
47	1.077

Strip number	Energy Resolution [%]
48	0.953
49	0.869
50	0.862
51	0.824
52	0.906
53	0.870
54	0.945
55	0.865
56	0.994
57	0.949
58	0.942
59	0.942
60	0.902
61	0.827
62	1.101
63	0.971

Table 6.8: Energy Resolution per strip for detector “‘DSSSD 21-5”

Strip number	Energy Resolution [%]
0	0.823
1	0.836
2	0.838
3	0.834
4	0.788
5	0.803
6	0.765
7	0.808
8	0.781
9	0.847
10	0.777
11	0.778
12	0.821
13	0.868
14	0.816
15	0.847

Strip number	Energy Resolution [%]
16	0.838
17	0.869
18	0.891
19	0.891
20	0.778
21	0.814
22	0.760
23	0.760
24	1.830
25	0.774
26	0.899
27	0.851
28	0.775
29	0.818
30	0.884
31	0.956

Strip number	Energy Resolution [%]
32	0.874
33	0.906
34	0.749
35	0.810
36	0.840
37	0.783
38	0.725
39	0.725
40	0.905
41	0.758
42	0.758
43	0.754
44	0.807
45	0.724
46	0.685
47	0.842

Strip number	Energy Resolution [%]
48	0.842
49	0.696
50	0.759
51	0.816
52	0.784
53	0.771
54	0.717
55	0.763
56	0.870
57	0.876
58	0.815
59	0.815
60	0.731
61	0.775
62	0.832
63	0.830

Table 6.9: Energy Resolution per strip for detector ”Wafer - 110”

Strip number	Energy Resolution [%]
0	0.867
1	0.772
2	0.844
3	0.826
4	0.800
5	0.841
6	0.854
7	0.839
8	0.815
9	0.861
10	0.825
11	0.868
12	0.857
13	0.806
14	0.828
15	0.768

Strip number	Energy Resolution [%]
16	0.812
17	0.809
18	0.894
19	0.894
20	0.854
21	0.790
22	0.903
23	0.903
24	1.839
25	0.823
26	0.773
27	0.781
28	0.788
29	0.848
30	0.870
31	0.961

Strip number	Energy Resolution [%]
32	0.875
33	0.880
34	0.709
35	0.766
36	0.742
37	0.824
38	0.829
39	0.750
40	0.805
41	0.789
42	0.789
43	0.848
44	0.756
45	0.748
46	0.712
47	0.731

Strip number	Energy Resolution [%]
48	0.731
49	0.785
50	0.738
51	0.725
52	0.784
53	0.779
54	0.805
55	0.761
56	0.762
57	0.748
58	0.752
59	0.752
60	0.793
61	0.640
62	0.831
63	0.717